

The impact of resistivity on the variability of black hole accretion flows

Antonios Nathanail^{1,2}, Yosuke Mizuno^{3,4,2}, Ioannis Contopoulos¹, Christian M. Fromm^{5,2,6}, Alejandro Cruz-Osorio⁷, Kotaro Moriyama^{8,2} and Luciano Rezzolla^{2,9,10}

¹ Research Center for Astronomy and Applied Mathematics, Academy of Athens, Athens 11527, Greece

² Institut für Theoretische Physik, Goethe Universität Frankfurt, Max-von-Laue-Str.1, 60438 Frankfurt am Main, Germany

³ Tsung-Dao Lee Institute, Shanghai Jiao Tong University, Shanghai 201210, China

⁴ School of Physics and Astronomy, Shanghai Jiao Tong University, Shanghai 200240, China

⁵ Institut für Theoretische Physik und Astrophysik, Universität Würzburg, Emil-Fischer-Strasse 31, 97074 Würzburg, Germany

⁶ Max-Planck-Institut für Radioastronomie, Auf dem Hügel 69, D-53121 Bonn, Germany

⁷ Instituto de Astronomía, Universidad Nacional Autónoma de México, AP 70-264, 04510 Ciudad de México, Mexico

⁸ Instituto de Astrofísica de Andalucía, Gta. de la Astronomía, s/n, Genil, 18008 Granada

⁹ School of Mathematics, Trinity College, Dublin 2, Ireland

¹⁰ Frankfurt Institute for Advanced Studies, Ruth-Moufang-Str. 1, 60438 Frankfurt am Main, Germany

Received July 15, 2024; Accepted November 19, 2024

ABSTRACT

Context. The accretion of magnetized plasma onto black holes is a complex and dynamic process, where the magnetic field plays a crucial role. The amount of magnetic flux accumulated near the event horizon significantly impacts the accretion flow behavior. Resistivity, a measure of how easily magnetic fields can dissipate, is thought to be a key factor influencing this process.

Aims. This work explores the influence of resistivity on accretion flow variability. We investigate simulations reaching the magnetically arrested disk (MAD) limit and those with an initial multi-loop magnetic field configuration.

Methods. We employ 3D resistive general relativistic magnetohydrodynamic (GRMHD) simulations to model the accretion process under various regimes, where resistivity has a global uniform value.

Results. Our findings reveal distinct flow behaviors depending on resistivity. High resistivity simulations never achieve the MAD state, indicating a disturbed magnetic flux accumulation process. Conversely, low resistivity simulations converge towards the ideal MHD limit. The key results are: i) For the standard MAD model, resistivity plays a minimal role in flow variability, suggesting that flux eruption events dominate the dynamics. ii) High resistivity simulations exhibit strong magnetic field diffusion into the disk, rearranging efficient magnetic flux accumulation from the accretion flow. iii) In multi-loop simulations, resistivity significantly reduces flow variability, which was not expected. However, magnetic flux accumulation becomes more variable due to frequent reconnection events at very low resistivity values.

Conclusions. This study shows that resistivity affects how much the flow is distorted due to magnetic field dissipation. Our findings provide new insights into the interplay between magnetic field accumulation, resistivity, variability and the dynamics of black hole accretion

Key words. black hole physics – resistivity – accretion – accretion discs – magnetic reconnection – magneto-hydrodynamics

1. Introduction

The accretion of plasma onto black holes is the basis for studying and analyzing observations of black holes. More specifically, the supermassive black hole, Sgr A*, located at the center of our galaxy, together with M87* have served as subjects for numerous multi-wavelength observation campaigns (Falcke et al. 1998; Baganoff et al. 2001; Genzel et al. 2003; Doeleman et al. 2008; Hada et al. 2013; Kim et al. 2018). The Event Horizon Telescope (EHT) Collaboration has recently achieved a remarkable milestone by capturing groundbreaking images of black holes, revealing a luminous ring surrounding a prominent black hole shadow (Event Horizon Telescope Collaboration et al. 2019a, 2022a) and an ordered magnetic field favouring the magnetically arrested disk MAD state (Event Horizon Telescope Collaboration et al. 2021, 2024). These observations highlight the limi-

tations of current theoretical models in explaining the variability observed in the light curves of these objects (Event Horizon Telescope Collaboration et al. 2022b). Understanding and characterizing this variability is essential for interpreting both black hole images and light curve data (Burke et al. 2021; Broderick et al. 2022; Georgiev et al. 2022; Satapathy et al. 2022).

MAD models are commonly used to describe active galactic nuclei (AGN) with jets (Bisnovatyi-Kogan & Ruzmaikin 1974; Narayan et al. 2003; Cruz-Osorio et al. 2022; Fromm et al. 2022). As accretion progresses, magnetic flux accumulates near the black hole's event horizon. The resulting magnetic pressure eventually balances the ram pressure of the disk, reaching equipartition and significantly impeding further accretion (Igumenshchev et al. 2003; Igumenshchev 2008; Tchekhovskoy et al. 2011). However, three-dimensional, non-axisymmetric processes, like the magnetic Rayleigh - Taylor instability, allow for continued accretion (Papadopoulos & Contopoulos 2019).

* anathanail@academyofathens.gr

Table 1. Initial parameters for the models considered

model	$\frac{2\rho_{\max}}{(B^2)_{\max}}$	$\sigma_{\max} \times 10^{-4}$	module	η 5×	$N_r \times N_\theta \times N_\phi$	r_{in}	r_{pmax}	r_{max}	$\langle Q_\theta \rangle$ < 4000 M	$\langle Q_\theta \rangle$ > 4000 M
MAD.S.100.E.00	100	2	Ideal	0	$384 \times 192 \times 192$	20	41	2500	>10	>10
MAD.S.100.E. – 6	100	2	Resistive	10^{-6}	$384 \times 192 \times 192$	20	41	2500	>10	3
MAD.S.26.E. – 6	26	4	Resistive	10^{-6}	$384 \times 192 \times 192$	20	41	2500	>10	6
MAD.S.26.E. – 5	26	4	Resistive	10^{-5}	$384 \times 192 \times 192$	20	41	2500	>10	6
MAD.S.26.E. – 5.HR	26	4	Resistive	10^{-5}	$1050 \times 768 \times 384$	20	41	500	>10	>10
MAD.S.26.E. – 4	26	4	Resistive	10^{-4}	$384 \times 192 \times 192$	20	41	2500	>10	>10
MAD.S.26.E. – 3	26	4	Resistive	10^{-3}	$384 \times 192 \times 192$	20	41	2500	>10	5
ML.S.26.E.00	26	2.5	Ideal	0	$1050 \times 768 \times 384$	6	12	500	>10	>10
ML.S.26.E. – 5	26	2.5	Resistive	10^{-5}	$1050 \times 768 \times 384$	6	12	500	>10	>10

Notes. The first column refers to the type of accretion model, whereas the second column to the initial maximum values of $2\rho/B^2$ and the third column to the initial maximum magnetization σ_{\max} . The fourth column corresponds to the module used in BHAC Ideal or Resistive and the next column to the value of the uniform resistivity η , employed (Ideal models have $\eta = 0$). The next column reports the resolution of each run, whereas columns 7 and 8 report the inner radius and maximum density radii of the torus, and the 9th column the outer radius of the domain, in units of r_g . The two last columns report the average MRI quality factor Q_θ at the heart of the torus (Event Horizon Telescope Collaboration et al. 2019b) for time before (column 10) and after 4000 M (last column)^a.

^a More details on the MRI quality factor can be found in Appendix C.

Resistivity plays a crucial role, by influencing the magnetic reconnection process itself. The angular momentum transport and the amplitude of magnetic energy after saturation can be significantly reduced by finite resistivity, as the Magneto-rotational Instability (MRI) can be influenced under certain conditions in the disk, which would affect the angular momentum transport (Pandey & Wardle 2012). A common approach is to introduce a global constant value for resistivity in relativistic MHD simulations (Del Zanna et al. 2016; Ripperda et al. 2019a; Mattia et al. 2023). However, a more realistic and physically motivated model for resistivity is needed, considering its non-uniform nature. Ideally, resistivity should be significant only on local scales, like X-points where reconnection occurs, while leaving the global dynamics largely unaffected ((Selvi et al. 2023)). A similar investigation took place a decade ago in pulsars but soon was replaced by Particle-in-cell simulations (Li et al. 2012; Kalapotharakos et al. 2012).

This study investigates the impact of resistivity on the dynamics of the accretion flow using a global prescription to describe this effect. We present results of 3D GRMHD simulations for resistive MAD models and also accretion models with an initial multi-loop magnetic field configuration, in which there is no steady magnetized funnel above the black hole but reconnecting current sheets are periodically formed in this region (Nathanail et al. 2020a; Chashkina et al. 2021; Nathanail et al. 2022b). The latter scenario may be specifically relevant for modeling the future observations of the galactic center, Sgr A* (Nathanail et al. 2022a). It is important to note that resistivity was thought not to have a significant impact on the variability of the accretion process, let alone reduce it. However, a key and unexpected result of our study is that the inclusion of resistivity does influence and even lower the variability for a specific accretion model, the multi-loop one.

The paper is structured as follows: In Section 2 we present our simulations, with subsection 2.1 focusing on the numerical setup and subsection 2.2 reporting the details of the accretion process. In subsection 2.3 we analyze and discuss the variability of the accretion flow, and in Section 3 we present our conclusions.

2. Resistive GRMHD simulations

2.1. Numerical setup

The numerical configuration comprises a Kerr black hole space-time and an initially perturbed torus infused with a poloidal magnetic field. All simulations conducted in this study are performed in three spatial dimensions, employing the GRMHD code BHAC (Porth et al. 2017). This code utilizes second-order shock-capturing finite-volume methods and has been extensively utilized in various investigations (Nathanail et al. 2019; Mizuno et al. 2018; Nathanail et al. 2020b). It employs the constrained-transport method (Del Zanna et al. 2007) to ensure a divergence-free magnetic field (Olivares et al. 2019) and has undergone comprehensive testing and comparisons with similar-capability GRMHD codes (Porth et al. 2019).

We explore two sets of models, MAD and multi-loop configurations. For the first, the initial data consist of an equilibrium torus with a constant specific angular momentum of $\ell = 6.76$ (Fishbone & Moncrief 1976) orbiting around a Kerr black hole with dimensionless spins of $a = 0.937$. The magnetic field is initialised as a nested loop described by the vector potential:

$$A_\phi = \max \left(\left(\frac{\rho}{\rho_{\max}} \left(\frac{r}{r_{\text{in}}} \right)^3 \sin^3 \theta \exp \left(\frac{-r}{400} \right) - 0.2, 0 \right), \quad (1)$$

where the maximum rest-mass density in the torus is denoted with ρ_{\max} .

For the multi-loop models for a spin of $a = 0.5$ and $\ell = 4.28$, the initial magnetic field consists of a series of nested loops with alternating polarity. The vector potential has the form:

$$A_\phi \propto \max \left(\frac{\rho}{\rho_{\max}} - 0.2, 0 \right) \cos((N-1)\theta) \sin \left(\frac{2\pi(r-r_{\text{in}})}{\lambda_r} \right), \quad (2)$$

the additional parameters ($N = 3$ and $\lambda_r = 2$) set the number and the characteristic length-scale of the initial magnetic loops in the torus. presented and analysed in 2D and 3D (Parfrey et al. 2015; Yuan et al. 2019a,b; Mahlmann et al. 2020). Two-temperature GRMHD simulations with a multi-loop magnetic field have also been conducted to trace electron heating through

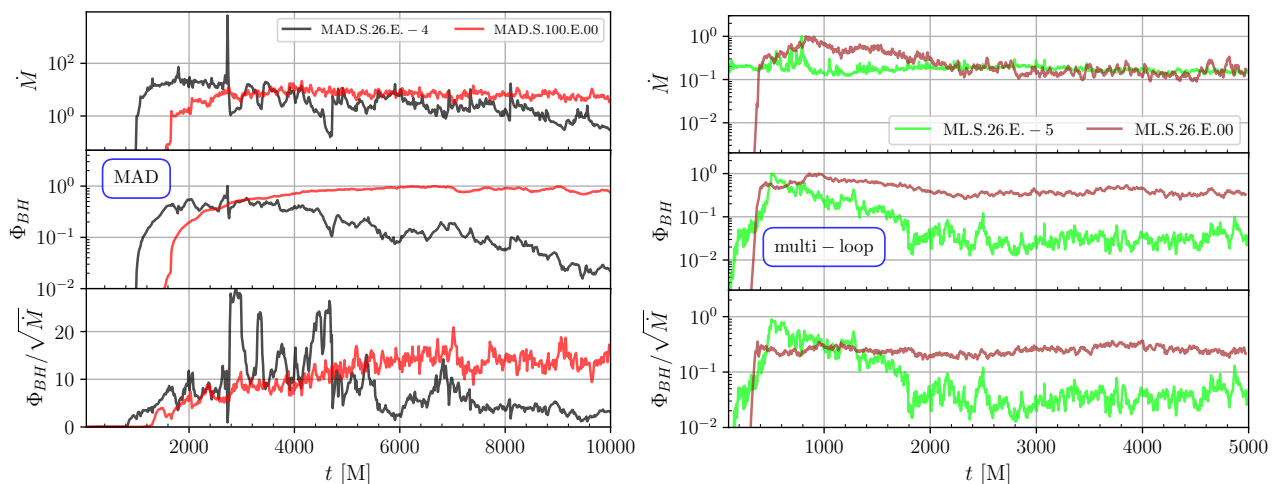


Fig. 1. Upper panels: mass accretion rate, \dot{M} , through the black-hole horizon, Middle panels: the magnetic flux accumulated on the black-hole horizon, Φ_{BH} , Lower panels: the normalized magnetic flux accumulated on the black-hole horizon, ϕ_{BH} . Left panels: MAD models. Right panels: multi-loop models in both panels ideal and resistive (see Table 1 for details.)

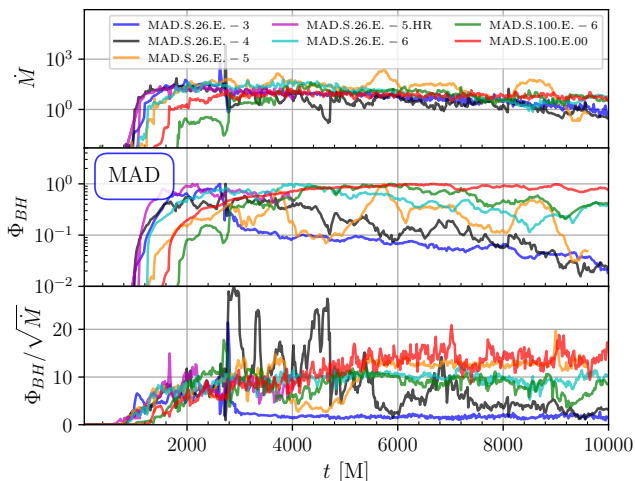


Fig. 2. Same as Fig. 1 for all MAD models (see Table 1 for details.)

turbulence and reconnection, with findings suggesting that the electrons are often trapped in plasmoids (Jiang et al. 2023). Additionally, these simulations investigated the emission properties of the plasmoids (Jiang et al. 2024).

The computational domain adopts a spherical logarithmic Kerr-Schild coordinate system. In Table 1 we report all the 3D simulations conducted in this study. The initial field strength is set by the value of $2p_{\max}/(B^2)_{\max}$, where the location of maximum of fluid and magnetic pressure may not coincide. The ideal MAD model, MAD.S.100.E.00, is the standard MAD model, typical in the literature, for comparison the same model is run with resistivity $\eta = 5 \times 10^{-6}$, MAD.S.100.E.-6. To study the effect of magnetic field dissipation and its impact on the dynamics of the flow we increase the field strength for the rest of the models which results in a factor of 2 larger initial maximum magnetization. The effective resolution is reported in column 6 of Table 1. Models MAD.S.26.E.-5.HR, ML.S.26.E.00 and ML.S.26.E.-5 that have the highest resolution, end at $t = 5000$ M.

For the simulations utilizing physical resistivity, i.e., $\eta \neq 0$, we employ the resistive GRMHD equations implemented in

BHAC (Ripperda et al. 2019a). In this setup, we assume a uniform and constant resistivity with a varying value of $\eta = 5 \times 10^{-3} - 10^{-6}$. The choice of a small resistivity, $\eta = 5 \times 10^{-5}$ and $\eta = 5 \times 10^{-6}$ is deliberate, as it allows us to replicate nearly ideal conditions for the accretion flow dynamics while also permitting physical magnetic reconnection processes that may lead to the formation of plasmoids (Ripperda et al. 2019b, 2020).

In jets of supermassive black holes, considering the gravitational radius, $L \approx r_g$, as the characteristic length scale, resistivity of $\eta = 5 \times 10^{-6}$ yields a high Lundquist number of $S := Lu_A/\eta = r_g c/\eta > 10^4$, magnetization is large and the Alfvén speed approaches the speed of light $u_A \approx c$ (Guo et al. 2015). This value represents the minimum Lundquist number required to generate plasmoids under the physical conditions examined in this study (Bhattacharjee et al. 2009; Uzdensky et al. 2010; Ripperda et al. 2019b, 2020). However, we also employ values of resistivity higher than the minimum value to explore its impact on the properties of the accretion flow and the induced variability.

In the ideal-GRMHD models (refer to Table 1), the dissipation of magnetic energy is solely a numerical effect. However, previous 2D simulations have demonstrated that, increasing the resolution still allows us to obtain physically meaningful results, allowing a more detailed study of the solution’s behavior (Obergaullinger et al. 2009; Rembiasz et al. 2017; Nathanail et al. 2020a; Obergaullinger & Aloy 2020).

2.2. Properties of the accretion flow

Our work primarily focuses on a single aspect, investigating the influence of resistivity on the variability of the accretion flow. To analyze the main properties of the accretion dynamics we define the rest-mass accretion rate and the magnetic flux across

¹ For Sgr A*, and a magnetic field of $B \approx 30$ G, resistivity is $\eta = \eta_{\text{code}} \times t_g$ s, thus $\eta = 5 \times 10^{-6} \times t_{g,\text{SgrA}^*} = 10^{-4}$ s in Gaussian/ESU units, for reference this value is well above the Spitzer resistivity ($\eta_{SP} = 1.15 \times 10^{-14} Z \ln \Lambda(T)^{-3/2} \approx 10^{-20}$ s, with $Z = 1$ for hydrogen, $\ln \Lambda$ the Coulomb logarithm and T the electron temperature) of the local plasma, but closer to the expected anomalous resistivity expected in astrophysical accretion disks

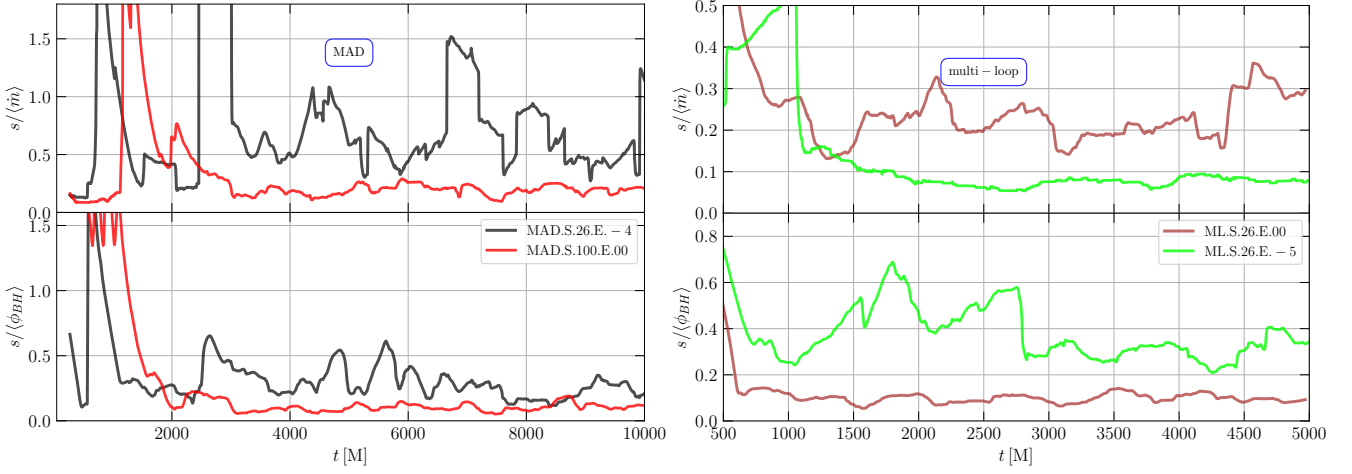


Fig. 3. Upper panels: the measure of variability for the mass accretion rate $s/\langle\dot{m}\rangle$, Lower panels: the measure of variability for the normalized magnetic flux accumulated on the black-hole horizon $s/\langle\phi_{BH}\rangle$, both for a time window of ± 270 M (Event Horizon Telescope Collaboration et al. 2022b). Left panels: All MAD models ideal and with different resistivity, Right panels: multi-loop models ideal and resistive (see Table 1 for details.)

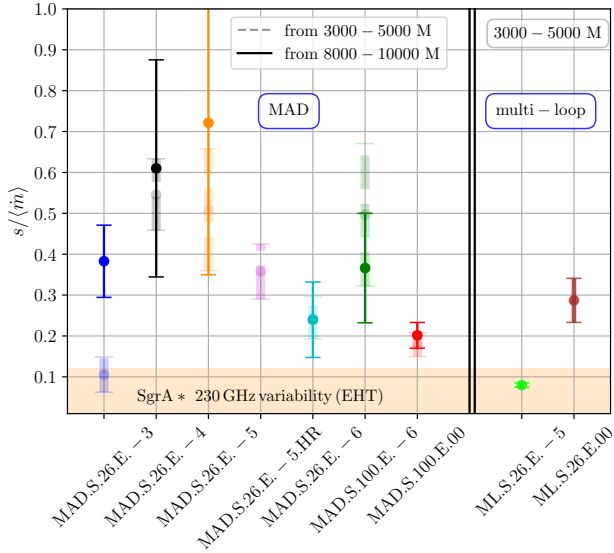


Fig. 4. The measure of variability for the mass accretion rate $s/\langle\dot{m}\rangle$, (error bars $\pm 1\sigma$) for all MAD and multi-loop models in time windows 3000 – 5000 M (dashed error bars) and 8000 – 10000 M (solid error bars) respectively.

the horizon. The former is measured as:

$$\dot{M} := \int_0^{2\pi} \int_0^\pi \rho u^r \sqrt{-g} d\theta d\phi, \quad (3)$$

where ρ is the rest-mass density, u^r is the radial component of the four-velocity and $\sqrt{-g}$ is the determinant of the spacetime metric. Its behaviour is reported as a function of time in the upper panels of Figs. 1 and 2. The left panels refer to two MAD models, whereas the right ones to the multi-loop models. The magnetic flux accreted across the event horizon is defined as:

$$\Phi_{BH} := \frac{1}{2} \int_0^{2\pi} \int_0^\pi |B^r| \sqrt{-g} d\theta d\phi, \quad (4)$$

while the “normalized” magnetic flux is defined as $\phi_{BH} := \Phi_{BH}/\sqrt{\dot{M}}$. In the middle (and lower) panels of Figs. 1 and 2

the magnetic flux (and normalized magnetic flux respectively) is shown for all of the models considered. The limiting normalized magnetic flux quoted by Tchekhovskoy et al. (2011) is $\phi_{BH} = \phi_{max} \approx 50$. In our simulations using Heaviside-Lorentz units (as opposed to Gaussian units) this value should be divided by a $\sqrt{4\pi}$, thus $\phi_{BH} = \phi_{max} \approx 50/\sqrt{4\pi} \approx 14$.

Accretion models with low resistivity ($\eta = 5 \times 10^{-5}$) exhibit a behavior consistent with standard MAD models. However, as resistivity increases ($\eta = 5 \times 10^{-4}$), the dynamics change. At $\eta = 5 \times 10^{-4}$, intense dissipation at the boundary of the magnetized funnel triggers a flare event lasting nearly 1000 M (left panels of Fig 1). This event leads to a sharp decrease in magnetic flux at the horizon. The simulation eventually settles into a state with a much lower flux level. A complete discussion of magnetic field accumulation in resistive MAD models can be found in Appendix A.

2.3. Variability of the accretion flow

To measure the variability of the accretion flow we define the mean and its variance for the quantities introduced before, namely the mass accretion rate and the normalized magnetic flux. The computation is done at a specific point in the time series for a window of ± 270 M², thus defined as follows:

$$\mu = \frac{1}{2n} \sum_{i=-n}^{+n} k_i, \quad s^2 = \frac{1}{2n} \sum_{i=-n}^{+n} (k_i - \mu)^2, \quad (5)$$

where $n = 270$ and k_i is the quantity under investigation, e.g., \dot{M} or ϕ_{BH} . Finally, we report the value of s/μ , where $\mu = \langle\dot{m}\rangle$ or $\langle\phi_{BH}\rangle$, which measures the variability for each of these quantities. In Fig. 3, we present the results of this procedure for the mass accretion rate (upper panels) and the normalized flux (lower panels) for two MAD models³ (in the left panel) and the multi-loop models (in the right panel).

The variability imprinted in the normalized magnetic flux is similar in the MAD models (left panel). More specifically, at late

² The time window was chosen to cover 3 hours of observational data for SgrA* see (Event Horizon Telescope Collaboration et al. 2022b) for details.

³ Variability for all MAD models is shown in the Appendix B.

times (8000 – 10000 M) it stabilizes around 0.2. Minimum variability occurs in the MAD model with $\eta = 5 \times 10^{-5}$. Intense reconnection near the horizon due to colliding flux tubes of opposite polarity significantly increases the variability of the normalized flux in the multi-loop models (Nathanail et al. 2022b).

Mass accretion rate, a measure of how much mass is falling on the black hole, plays a crucial role in shaping the radiation light-curve, particularly at 230 GHz. Studies have shown a close link between the variability of mass accretion rate and the variability of the light-curve at 230 GHz (Porth et al. 2019; Chatterjee et al. 2021). For this reason we primarily focus on the variability of the mass accretion rate.

The results of the mean variability are summarised in Fig. 4 for two different time windows, namely 3000 – 5000 M and 8000 – 10000 M. Variability is significantly reduced by the inclusion of resistivity only for the multi-loop model. For models capable of reaching the MAD state, the variability is not influenced significantly by the inclusion of resistivity. However, there is no simple relation between the variability of the flow and the resistivity of the plasma, as seen in Fig. 4. A proper analysis of the 230 GHz light curve, which is the EHT’s target frequency, will be conducted in future studies.

3. Conclusions

The key findings are the following:

1. For MAD models, resistivity of $\eta = 5 \times 10^{-5} - 10^{-6}$ has minimal impact on the variability of the flow, indicating that the dynamics are primarily driven by magnetic flux eruption events.
2. For MAD models, simulations with resistivity of $\eta = 5 \times 10^{-3} - 10^{-4}$, show significant magnetic field diffusion into the disk, hindering the efficient accumulation of magnetic flux from the accretion flow.
3. For multi-loop models, even if frequent reconnection events lead to increased variability in magnetic flux accumulation, resistivity significantly reduces the variability of the accretion flow. We need here to stress out that resistivity was not expected to have such an impact.

Acknowledgements. Support comes from the ERC Advanced Grant “JETSET: Launching, propagation and emission of relativistic jets from binary mergers and across mass scales” (Grant No. 884631). YM is supported by the National Key R&D Program of China (grant no. 2023YFE0101200), the National Natural Science Foundation of China (grant no. 12273022), and the Shanghai municipality orientation program of basic research for international scientists (grant no. 22JC1410600). CMF is supported by the DFG research grant “Jet physics on horizon scales and beyond” (Grant No. 443220636) within the DFG research unit “Relativistic Jets in Active Galaxies” (FOR 5195). ACO gratefully acknowledges “Ciencia Básica y de Frontera 2023-2024” program of the “Consejo Nacional de Humanidades, Ciencias y Tecnología” (CONAHCYT, Mexico) project CBF2023-2024-1102 and SNI 257435. This work was supported by computational time granted from the National Infrastructures for Research and Technology S.A. (GRNET S.A.) in the National HPC facility - ARIS - under project ID 16033. Simulations were performed also on SuperMUC at LRZ in Garching, on the GOETHE-HLR cluster at CSC in Frankfurt, and on the HPE Apollo Hawk at the High Performance Computing Center Stuttgart (HLRS).

Data Availability. The data underlying this article will be shared on reasonable request to the corresponding author.

References

Baganoff, F. K., Bautz, M. W., Brandt, W. N., et al. 2001, *Nature*, 413, 45
Bhattacharjee, A., Huang, Y.-M., Yang, H., & Rogers, B. 2009, *Physics of Plasmas*, 16, 112102

Bisnovatyi-Kogan, G. S. & Ruzmaikin, A. A. 1974, *Astrophysics and Space Science*, 28, 45
Broderick, A. E., Gold, R., Georgiev, B., et al. 2022, *Astrophys. J. Lett.*, 930, L21
Burke, C. J., Shen, Y., Blaes, O., et al. 2021, *Science*, 373, 789
Chashkina, A., Bromberg, O., & Levinson, A. 2021, arXiv e-prints, arXiv:2106.15738
Chatterjee, K., Markoff, S., Neilsen, J., et al. 2021, *Mon. Not. R. Astron. Soc.*, 507, 5281
Cruz-Ororio, A., Fromm, C. M., Mizuno, Y., et al. 2022, *Nature Astronomy*, 6, 103
Del Zanna, L., Papini, E., Landi, S., Bugli, M., & Bucciantini, N. 2016, *Mon. Not. R. Astron. Soc.*, 460, 3753
Del Zanna, L., Zanotti, O., Bucciantini, N., & Londrillo, P. 2007, *Astron. Astrophys.*, 473, 11
Doelman, S. S., Weintraub, J., Rogers, A. E. E., et al. 2008, *Nature*, 455, 78
Event Horizon Telescope Collaboration, Akiyama, K., Alberdi, A., et al. 2022a, *Astrophys. J. Lett.*, 930, L12
Event Horizon Telescope Collaboration, Akiyama, K., Alberdi, A., et al. 2019a, *Astrophys. J. Lett.*, 875, L1
Event Horizon Telescope Collaboration, Akiyama, K., Alberdi, A., et al. 2022b, *Astrophys. J. Lett.*, 930, L16
Event Horizon Telescope Collaboration, Akiyama, K., Algaba, J. C., et al. 2021, *Astrophys. J. Lett.*, 910, L13
Event Horizon Telescope Collaboration, Akiyama, K., et al. 2024, *Astrophys. J. Lett.*, 964, L26
Event Horizon Telescope Collaboration, Porth, O., et al. 2019b, *Astrophys. J. Supp.*, 243, 26
Falcke, H., Goss, W. M., Matsuo, H., et al. 1998, *Astrophys. J.*, 499, 731
Fishbone, L. G. & Moncrief, V. 1976, *Astrophys. J.*, 207, 962
Fromm, C. M., Cruz-Ororio, A., Mizuno, Y., et al. 2022, *Astron. Astrophys.*, 660, A107
Genzel, R., Schödel, R., Ott, T., et al. 2003, *Nature*, 425, 934
Georgiev, B., Pesce, D. W., Broderick, A. E., et al. 2022, *Astrophys. J. Lett.*, 930, L20
Guo, F., Liu, Y.-H., Daughton, W., & Li, H. 2015, *Astrophys. J.*, 806, 167
Hada, K., Kino, M., Doi, A., et al. 2013, *Astrophys. J.*, 775, 70
Igumenshchev, I. V. 2008, *Astrophys. J.*, 677, 317
Igumenshchev, I. V., Narayan, R., & Abramowicz, M. A. 2003, *Astrophys. J.*, 592, 1042
Jiang, H.-X., Mizuno, Y., Dihingia, I. K., et al. 2024, arXiv e-prints, arXiv:2404.03237
Jiang, H.-X., Mizuno, Y., Fromm, C. M., & Nathanail, A. 2023, *Mon. Not. R. Astron. Soc.*, 522, 2307
Kalapotharakos, C., Harding, A. K., Kazanas, D., & Contopoulos, I. 2012, *Astrophys. J. Lett.*, 754, L1
Kim, J., Marrone, D. P., Roy, A. L., et al. 2018, *The Astrophysical Journal*, 861, 129
Li, J., Spitkovsky, A., & Tchekhovskoy, A. 2012, *Astrophys. J.*, 746, 60
Mahlmann, J. F., Levinson, A., & Aloy, M. A. 2020, *Mon. Not. R. Astron. Soc.*, 494, 4203
Mattia, G., Del Zanna, L., Bugli, M., et al. 2023, *Astron. Astrophys.*, 679, A49
Mizuno, Y., Younsi, Z., Fromm, C. M., et al. 2018, *Nature Astronomy*, 2, 585
Narayan, R., Igumenshchev, I. V., & Abramowicz, M. A. 2003, *Publications of the ASJ*, 55, L69
Nathanail, A., Dhang, P., & Fromm, C. M. 2022a, *Mon. Not. R. Astron. Soc.*, 513, 5204
Nathanail, A., Fromm, C. M., Porth, O., et al. 2020a, *Mon. Not. R. Astron. Soc.*, 495, 1549
Nathanail, A., Gill, R., Porth, O., Fromm, C. M., & Rezzolla, L. 2020b, *Mon. Not. R. Astron. Soc.*, 495, 3780
Nathanail, A., Mpisketzis, V., Porth, O., Fromm, C. M., & Rezzolla, L. 2022b, *Mon. Not. R. Astron. Soc.*, 513, 4267
Nathanail, A., Porth, O., & Rezzolla, L. 2019, *Astrophys. J. Lett.*, 870, L20
Obergaullinger, M. & Aloy, M. Á. 2020, in *Journal of Physics Conference Series*, Vol. 1623, *Journal of Physics Conference Series*, 012018
Obergaullinger, M., Cerdá-Durán, P., Müller, E., & Aloy, M. A. 2009, *Astron. Astrophys.*, 498, 241
Olivares, H., Porth, O., Davelaar, J., et al. 2019, *Astron. Astrophys.*, 629, A61
Pandey, B. P. & Wardle, M. 2012, *Mon. Not. R. Astron. Soc.*, 423, 222
Papadopoulos, D. B. & Contopoulos, I. 2019, *Mon. Not. R. Astron. Soc.*, 483, 2325
Parfrey, K., Giannios, D., & Beloborodov, A. M. 2015, *Mon. Not. R. Astron. Soc.*, 446, L61
Porth, O., Chatterjee, K., Narayan, R., et al. 2019, *Astrophys. J. Supp.*, 243, 26
Porth, O., Olivares, H., Mizuno, Y., et al. 2017, *Computational Astrophysics and Cosmology*, 4, 1
Rembiasz, T., Obergaullinger, M., Cerdá-Durán, P., Aloy, M.-Á., & Müller, E. 2017, *Astrophys. J., Supp.*, 230, 18
Ripperda, B., Bacchini, F., & Philippov, A. A. 2020, *Astrophys. J.*, 900, 100

- Ripperda, B., Bacchini, F., Porth, O., et al. 2019a, *Astrophys. J., Supp.*, 244, 10
Ripperda, B., Porth, O., Sironi, L., & Keppens, R. 2019b, *Mon. Not. R. Astron. Soc.*, 485, 299
Satapathy, K., Psaltis, D., Özel, F., et al. 2022, *Astrophys. J.*, 925, 13
Selvi, S., Porth, O., Ripperda, B., et al. 2023, *Astrophys. J.*, 950, 169
Siegel, D. M., Ciolfi, R., Harte, A. I., & Rezzolla, L. 2013, *Phys. Rev. D* R, 87, 121302
Takahashi, R. 2008, *Mon. Not. R. Astron. Soc.*, 383, 1155
Tchekhovskoy, A., Narayan, R., & McKinney, J. C. 2011, *Mon. Not. R. Astron. Soc.*, 418, L79
Uzdensky, D. A., Loureiro, N. F., & Schekochihin, A. A. 2010, *Phys. Rev. Lett.*, 105, 235002
Yuan, Y., Blandford, R. D., & Wilkins, D. R. 2019a, *Mon. Not. R. Astron. Soc.*, 484, 4920
Yuan, Y., Spitkovsky, A., Blandford, R. D., & Wilkins, D. R. 2019b, *Mon. Not. R. Astron. Soc.*, 487, 4114

Appendix A. Magnetic field accumulation in Resistive MAD simulations

To better understand the dependence of simulation results on resistivity, Fig. 5 shows the average normalized magnetic flux on the horizon for all MAD models. The averages are taken over two-time windows: 3000–5000 M and 3000–10000 M. The figure clearly shows the flaring event for model MAD.S.26.E. – 4, where the flux fluctuates near the MAD limit in the first window and then drops slightly. Model MAD.S.26.E. – 3 shows a substantially lower flux already in the first window, indicating a clear deviation from typical MAD behavior. Longer simulations could highlight

Resistivity significantly impacts magnetic flux accumulation in MAD simulations due to energy dissipation at the edge of the magnetized funnel. Models with a rather low resistivity ($\eta = 5 \times 10^{-5}$) exhibit a behavior consistent with standard MAD models. At the highest resistivity run MAD.S.26.E. – 3 the system settles quickly into a state with very low magnetic flux on the horizon (see left, upper and bottom panels of Fig 2).

The effect of numerical resolution was compared in two simulations with $\eta = 5 \times 10^{-5}$, where the high-resolution run is indicated as HR, MAD.S.26.E. – 5.HR'. The higher resolution allows for a more accurate representation of small-scale physical processes, such as reconnection events at current sheets. As a consequence, the HR simulation exhibits more efficient magnetic energy dissipation near the edge of the funnel, resulting in a lower average accumulated flux compared to the standard resolution simulations. However, a definitive conclusion on the quantitative impact of resolution would require running the HR simulations for a longer time to ensure we capture the behavior of the system till 10000 M. In general, longer simulations could highlight whether our results remain consistent or change over extended time evolution.

Models with $\eta = 5 \times 10^{-6}$, suggest that a stronger initial magnetic field (in cyan, initial $\beta = 26$) allows the system to accumulate more flux faster and reach a state closer to the ideal MAD limit even in the presence of some resistivity. This com-

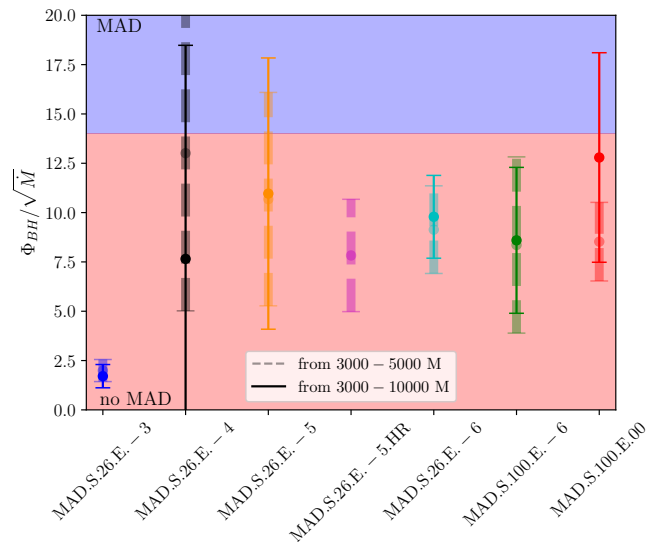


Fig. 5. The mean normalized magnetic flux accumulated on the black-hole horizon (error bars indicate $\pm 1s$) for all MAD models in time windows 3000–5000 M (dashed error bars) and 3000–10000 M (solid error bars) respectively. The dashed horizontal line depicts the MAD saturation value $\phi_{\max} \approx 50/\sqrt{4\pi} \approx 14$.

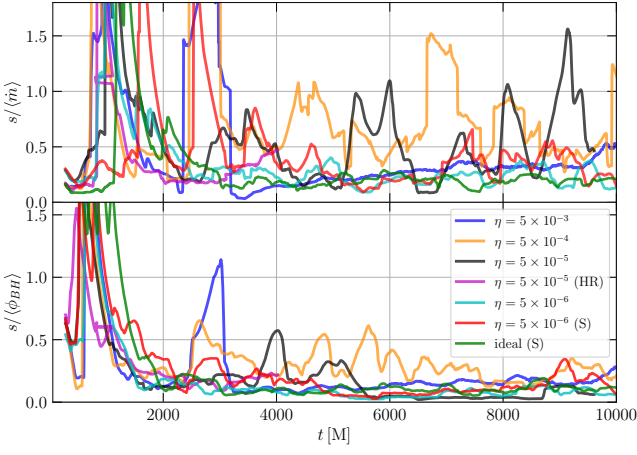


Fig. 6. Upper panels: the measure of variability for the mass accretion rate $s/\langle\dot{m}\rangle$, Lower panels: the measure of variability for the normalized magnetic flux accumulated on the black-hole horizon $s/\langle\phi_{BH}\rangle$, both for a time window of ± 270 M (Event Horizon Telescope Collaboration et al. 2022b) for all MAD models ideal and with different resistivity (see Table 1 for details.)

ment must be the same for all models, meaning that initialization with higher σ will eventually bring more magnetic flux at the event horizon. The simulations reveal that resistivity plays a crucial role in magnetic flux accumulation. Lower resistivity allows for behavior consistent with the standard MAD model. However, as resistivity increases, dissipation processes become more prominent, leading to flare events and a significant reduction in the accumulated magnetic flux.

Appendix B. Variability for all MAD models

In this Appendix we provide details for the variability of all MAD models in our study. Fig. 6 presents the results for $s/\langle\dot{m}\rangle$ (upper panel) and $s/\langle\phi_{BH}\rangle$ (lower panel) for a time window of ± 270 M (Event Horizon Telescope Collaboration et al. 2022b).

The model with the highest resistivity of $\eta = 5 \times 10^{-3}$ (MAD.S.26.E. – 3, blue line), exhibits a large bump at early times (3000 – 3500 M) likely corresponding to a rapid loss of magnetic flux. This is followed by a minimum variability state, which then steadily increases until the end of the simulation. Model MAD.S.26.E. – 4, which has a lower resistivity ($\eta = 5 \times 10^{-4}$, orange line) shows a similar initial variability bump and continues to exhibit recurring bumps every 1000 – 2000 M.

As is seen in models MAD.S.26.E. – 5 and MAD.S.26.E. – 5.HR, higher resolution reduces the numerical diffusion and let only the physical resistivity to act. Another point to make for the HR run is that it reduces slightly the variability in the first window, this was expected since having HR will impact any variability imposed from reconnection events. Further reducing the resistivity to $\eta = 5 \times 10^{-6}$, results in a similar level of variability to the standard ideal MAD model.

Appendix C. Variability of the Power of the jet

In this appendix we explore the variability on the jet power. For the multi-loop models such discussion does not make much sense, since it has been shown that there is no production of a

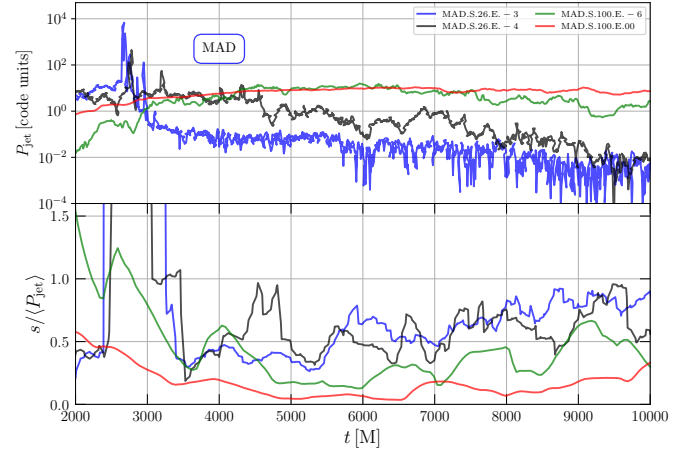


Fig. 7. Upper panels: The power of the jet as defined in Eq. (6) in code units. Lower panel: the measure of variability for the jet power for four representative MAD models.

steady jet (Nathanail et al. 2020a). Multi-loop models exhibit periodic outbursts either from the upper or the lower hemisphere. Thus, the variability of the jet power will be discussed only for MAD models.

The power is measured through the energy flux that passes through a 2-sphere placed at $50 r_g$. It is defined as follows:

$$P_{\text{jet}} := \int_0^{2\pi} \int_0^\pi (-T_t^r - \rho u^r) \sqrt{-g} d\theta d\phi, \quad (6)$$

where the integrand in (6) is set to zero everywhere on the integrating surface where $\sigma \leq 1$, in order to account only for the jet component.

The power of the jet of four MAD models is shown in the upper panel of Fig. 7. The ideal MAD model, MAD.S.100.E.00, has a similar power output with the low resistivity model, MAD.S.100.E. – 6. However, when the resistivity increases significantly the picture vastly changes. For models MAD.S.26.E. – 3 and MAD.S.26.E. – 4, there is an initial jump at the normalized magnetic flux at around 2500 M (see Fig. 2). A similar behavior is seen in the jet power, with an early burst followed by a steady decline in power throughout the simulation time.

To measure the variability of the jet power we make use of Eq. (5), where $k_i = P_{\text{jet}}$ in this case. The ideal model shows the smallest variability on the jet power, whereas all the rest resistive models, shown in the lower panel of Fig. 7, exhibit larger variability.

Appendix D. MRI quality factor Q_θ

We provide here the definition of the MRI quality factor Q_θ and details on its calculation presented in Table 1. We evaluate the so-called ‘‘quality factor’’ Q_θ , in terms of the ratio between the grid spacing in a given direction Δx_θ , (e.g., the θ -direction) and the wavelength of the fastest growing MRI mode in that direction (i.e., λ_θ), where both quantities are evaluated in the tetrad basis of the fluid frame $e_\mu^{(\hat{a})}$ (see Takahashi 2008; Siegel et al. 2013; Porth et al. 2019, for details)

$$Q_\theta := \frac{\lambda_\theta}{\Delta x_\theta}, \quad (7)$$

where

$$\lambda_\theta := \frac{2\pi}{\sqrt{(\rho h + b^2)}\Omega} b^\mu e_\mu^{(\theta)}, \quad (8)$$

$\Omega := u^\phi/u^t$ is the angular velocity of the fluid and the corresponding grid resolution is $\Delta x_\theta := \Delta x^\mu e_\mu^{(\theta)}$. Finally the average of Q_θ is done in space and time, specifically in a time window of 200 M and spatially in the region of interest at angles $60^\circ < \theta < 120^\circ$ and $r < 40 r_g$, inside the heart of the disk.